Optics & Laser Technology 174 (2024) 110552

Contents lists available at ScienceDirect

Optics and Laser Technology

journal homepage: www.elsevier.com/locate/optlastec

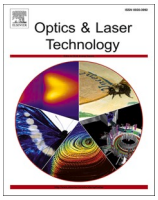

A tunable multitasking renal function assessment biosensor predicated on cylindrical metastructure

Jun-Yang Sui [a], Jia-Hao Zou [a], Ding-Yuan Zhang [b], Si-Yuan Liao [a], Yu-Xin Wei [a], Hai-Feng Zhang [a,*]

[a] College of Electronic and Optical Engineering & College of Flexible Electronics (Future Technology), Nanjing University of Posts and Telecommunications, Nanjing 210023, China
[b] School of Communications and Information Engineering, Nanjing University of Posts and Telecommunications (NJUPT), Nanjing 210023, China

ARTICLE INFO

Keywords:
Renal function assessment
Cylindrical metastructure
Glucose concentration
Serum creatinine concentration
Tunable

ABSTRACT

Chronic renal disease has become one of the world's most serious public health problems in recent decades, leading to physical degradation, and even death. Glucose and creatinine in body fluids are important indicators used to assess renal dysfunction, but current biosensors only focus on the detection and performance improvement of a single indicator. To break through the idea limitation, a cylindrical metastructure based on indium antimonide material is proposed in this paper. It innovatively realizes the tunable multitasking renal function assessment biosensor, which is more suitable for the application of multiple medical detection scenarios. Through the control of the external magnetic field strength, the glucose concentration of 0 ~ 400 g/L and the serum creatinine concentration of 80.9 ~ 85.28 μmol/L can be separately detected in real-time, unlabeled, and non-destructively, which own better performance than previous renal function assessment biosensors in terms of detection range, R^2, quality factor, figure of merit, and detection limit. This proposal has important reference value for promoting the detection and treatment of renal diseases, and the research of multitasking biosensors.

1. Introduction

Chronic renal disease has become a global public health problem [1,2], placing a huge strain on the global economy [3,4], and was the eighth leading cause of death in 2007 [5]. Under normal circumstances, the production of glucose and creatinine in our daily lives is at a relatively constant rate. Almost all glucose and creatinine are filtered through the glomerulus [6], and the levels of blood glucose concentration and serum creatinine concentration (C_C) are kept in a stable range. When the renal is dysfunctional and secretory capacity is impaired, blood glucose concentration and C_C will exceed the maximum physiological range [7]. Therefore, in clinical practice, measurements of blood glucose and C_C are useful biomarkers for the detection, disease staging, and monitoring of renal disease [8,9].

As the main component of human blood glucose [10], the refractive index (RI) change of glucose aqueous solution is close to that of blood glucose concentration [11]. The accurate detection of glucose concentration (C_G) provides a certain basis for the study of the latter. The conventional method is to use a test strip to analyze C_G in urine by observing changes in the strip color [12], but its results are inaccurate due to airborne or finger-borne contamination. In recent years, optical biosensors have been developed with the advantages of real-time detection, non-contact, and high sensitivity (S). Chamoli et al. [13] proposed an infrared C_G-sensitive biosensor, having a high S of 22 THz/RIU and a quality factor (Q) of 800. However, its figure of merit (FOM) of 0.3865 RIU^{-1} is very low, causing a noticeable degradation in the reflectance peak as the RI changes. This is not conducive to accurate observation. Ghorbani et al. [11] reported a plasma ring nanobiosensor for detecting C_G with a high S = 36 THz/RIU. However its Q of 16.5 was very low, and the detection limit (DL) was high, which made the absorption peak (AP) used for detection difficult to distinguish and brought inconvenience to the measurement. C_G biosensor performance with high Q, FOM, and low DL is an important reference for diagnosing blood glucose concentration to assess renal function. Creatinine, as a waste product of muscle and protein metabolism [14], is extracted from the blood by the kidneys and excreted in the urine. When the renal does not work properly, the creatinine level in the blood increases. Hence, monitoring serum C_C is crucial in gaining preliminary knowledge of

* Corresponding author.
E-mail addresses: hanlor@163.com, hanlor@njupt.edu.cn (H.-F. Zhang).

https://doi.org/10.1016/j.optlastec.2024.110552
Received 26 August 2023; Received in revised form 2 December 2023; Accepted 19 December 2023
Available online 13 January 2024

Table 1
The multitasking biosensing performance of the CMS.

B	Analyte	Range	S	R^2	Q	FOM	DL
0 T	C_G	0 ~ 400 g/L	0.03664 α/RIU	0.9995	666.46	61.96 RIU^{-1}	8.08×10^{-4} RIU
1.62 T	C_C	80.9 ~ 85.28 μmol/L	0.005859 α/RIU	0.9961	11126.23	139.97 RIU^{-1}	3.7×10^{-4} RIU

renal function. Alternative analytical techniques, such as gas or liquid chromatography-coupled mass spectrometry, are used to determine C_C in clinical laboratories [15]. However, these alternative methods are costly, time-consuming, and require pretreatment of the sample [15]. Therefore optical C_C biosensors with compact structure, real-time response, and easy operation are favored. Aly et al. [16] designed a novel biosensor predicated on one-dimensional planar photonic crystals for detecting C_C in blood. In the detection range of 80.9 ~ 85.28 μmol/L, the S was 306.25 nm/RIU. However, its reliability evaluation index of linear fitting R^2 was only 0.9132, indicating a significant deviation between the fitted equation and the actual measurement date. Hence, on the basis of high Q and FOM values, high R^2 is also an important standard for biosensors to have accurate and reliable detection capabilities.

Cylindrical metastructure (CMS) is an artificial dielectric topology that has the ability to control the frequency, polarization, and phase of electromagnetic waves (EWs), which is a physical property that natural structures do not have [17]. In addition, compared with plane geometry, cylindrical geometry has higher performance [18], so CMS has advantages in improving lateral propagation constraints, generating a complete band gap, and increasing light extraction rate [18], it also can achieve single-negative properties like chiral molecules [19–21]. Moreover, the new geometry can increase the possibility of CMS being used in biomedical and engineering applications [22]. However, the biggest preponderance of CMS is its ability to be combined with optical fibers, leading to the creation of metastructure fibers. Compared with ordinary fiber, the significant advantage of metastructure fiber is its structural diversity, and it has outstanding performance in many aspects, such as the properties of permanent adjustable dispersion, single-mode transmission, and high birefringence [23]. Thanks to these advantages, sensors based on CMS have become a research hotspot in the detection field in recent years. Gandhi et al. [22] designed a novel one-dimensional defective CMS biosensor based on porous silicon, capable of detecting very small changes in RI of different serum C_C samples, with S of 640.29 nm/RIU, Q of 1.15×10^5, and FOM of 2.6×10^4 RIU^{-1}. Abadla et al. [24] proposed a high-performance one-dimensional defect CMS temperature sensor and studied the thermal characteristics of the defect mode in the visible light region in the transmission spectrum, which could realize the detection of S = 11 nm/1000℃ in the ultra-wide temperature *T* range of 0 ~ 1000 ℃. Mehaney et al. [25] theoretically discussed a CMS design for biomedical fluid sensing and detection based on RI changes in the range of 1 ~ 1.5. The detection formant was formed by metal-induced Tamm/Fano states, achieving RI detection with S of 6770 nm/RIU and Q of 662. Although the above sensors predicated on CMS have excellent detection performance, they are only limited to the improvement of a single function, which restricts the development of ideas in related fields to a certain extent. As a narrow-band semiconductor with high mobility, indium antimonide (InSb) is highly dependent on magnetic field strength *B* in the range from infrared to microwave [26]. Therefore, InSb is often introduced into designed structures to enable them to be tuned by *B* [27]. For the last few years, planar metastructures based on InSb have been used to design tunable logic gates [28], physical quantity sensors [29], and magnetic control isolators [30] with excellent performance. In view of this, the introduction of InSb into CMS will give the CMS the

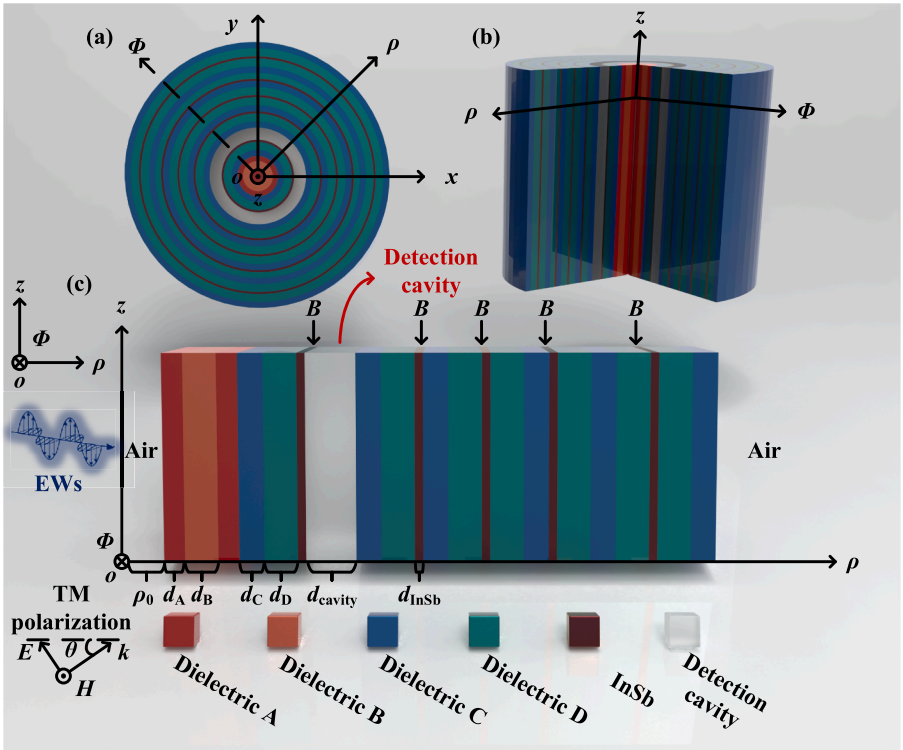

Fig. 1. Schematic diagrams of the CMS. (a) Top view of the CMST, (b) the front section view of the CMS, and (c) the cross-sectional view of the CMS on the ρoz plane along the $+\rho$-axis direction. The overall structure is composed of different dielectrics asymmetrically arranged, ABACDInSbCavity(CDInSb)^{2}DCInSbDCDInSbDC, where the Cavity symbolizes the detection cavity. For reference, coordinate axes are used to mark the propagation directions of the EWs and *B*.

ability to control the electromagnetic characteristics of the propagation EWs by tuning B, which provides an idea for the research of tunable multitasking biosensors predicated on CMS and is more suitable for the application of multiple biosensing scenarios.

In this paper, a tunable multitasking renal function assessment biosensor predicated on CMS is proposed, which has the advantages of compact structure, real-time detection, and non-contact. Through the introduction of the defects, the located detect mode resonance (LDMR) is excited, generating the sharp AP. By locking the frequency points corresponding to AP, CMS can realize RI detection. The introduction of InSb gives CMS the ability to utilize the B to tune the electromagnetic properties of EWs. Through the method of searching for optimization and reasonable structure construction, the absence of a magnetic field ($B = 0$ T) and the presence of a magnetic field ($B = 1.62$ T) can adjust the range of RI detection. Therefore, biosensing of C_G and C_C with different RI ranges is satisfied (see Table 1). Compared with previous renal function assessment biosensors [11,13,16], C_G and C_C detected through the designed CMS have a wider detection range, more reliable R^2, higher Q, FOM, and lower DL. This multitasking renal function assessment biosensor not only makes use of the geometric and optical properties of CMS, which is more conducive to biomedical detection but also supplements the traditional single-function biosensor, which has certain prospects in the application field of multi-scene medical detection. It should be emphasized that this work only focuses on theoretical innovation research of the ideal structure, and experiments are not included in the scope of this work due to a lack of funding and experimental environment.

2. Theoretical model

Through integrating the methods of planar metastructure and non-magnetized CMS, the transfer matrix equation of CMS is deduced [31,32]. The model diagrams of CMS are displayed in Fig. 1, which is formed by the asymmetric arrangement of common dielectrics A, B, C, and D filled with different colors, detection cavity, and the anisotropic dielectric InSb. For the actual fabrication of CMC, Refs. [33,34] propose the use of the etching method to precisely manufacture annular dielectric layer arrangement devices (see the detailed manufacturing procedure in Supporting Information). To adapt to general conditions, CMS is exposed to air (RI of 1) with radii of ρ_0 and ρ_f in the inner and outer layers, respectively. The operating T is selected to be 273 K. Considering the generality of the results, d is set to a normalized thickness of $d = 10$ μm. Additionally, the angular frequency ω is normalized to $\omega = 2\pi c/d$, denoted as α, where c is the speed of light in a vacuum. After the method of searching for optimization and reasonable structural design, the corresponding thickness of each dielectric layer is determined as $d_A = 0.25d$, $d_B = 0.38d$, $d_C = 0.289d$, $d_D = 0.4d$, and $d_{InSb} = 0.083d$. The radius of the inner air is $\rho_0 = 0.07d$. The RI of common dielectrics A, B, C, and D are $n_A = 3.7$, $n_B = 3.2$, $n_C = 2.75$, and $n_D = 2.78$, respectively. It is worth emphasizing that Leiwin et al. [35] deduced the expressions of effective permeability and permittivity of composite materials predicated on Mie resonance theory so that the RI required in this paper can be satisfied in a wide range. This technique has been practically applied (see Supporting Information for the detailed Mie resonance theory formula derivation) [36]. A cavity set as a detection cavity ($d_{cavity} = 0.54d$) is placed into the CMS for biosensing. When biosensing is used to detect C_G and C_C, inject the analyte into the detection cavity for RI detection with a precise technique based on micro-infiltration technology by hollow submicron-size pipettes [37].

In Fig. 1(c), EWs are entering the cylinder from its interior, the incident direction of the wave vector k is represented by arrow direction, and the incident angle θ is formed at the Φoz plane. EWs are vertically incident into the Φoz plane, $\theta = 0°$. Moreover, as shown in Fig. 1(c), the external magnetic field strength B is exerted perpendicular to the InSb layers in the direction of the -z-axis. In this paper, the electric field vectors belonging to the transverse magnetic (TM) polarization and transverse electric (TE) polarization are set along the $+\Phi$-axis and $+z$-axis, respectively. During EWs propagating in CMS, influenced by Lorentz force, B mainly regulates EWs under TM polarization, while EWs under TE polarization are not modulated by B [38]. Hence, the performance of CMS under TM polarization is only focused on in this work and the entire structure is analyzed by utilizing the transfer matrix method.

By integrating Maxwell's system of equations with the equation governing the motion of charged particles, the following expressions can be derived [39]:

$$\frac{d\boldsymbol{J}}{dt} + v\boldsymbol{J} - \omega_c \times \boldsymbol{J} = \varepsilon_0 \omega_p^2 E, \tag{1}$$

$$-\nabla \times E = \mu_0 \frac{\partial H}{\partial t}, \tag{2}$$

$$\nabla \times H = \varepsilon_0 \frac{\partial E}{\partial t} + \boldsymbol{J}, \tag{3}$$

where ε_0 and μ_0 respectively symbolize permittivity and permeability in the vacuum and $J = J_\rho + J_\varphi + J_z$ is the density arising from polarization [39]:

$$\begin{cases} (-jw + v)J_z = \varepsilon_0 \omega_p^2 E_z \\ (-jw + v)J_\rho + J_\phi \omega_c = \varepsilon_0 \omega_p^2 E_\rho \\ (-jw + v)J_\phi - J_\rho \omega_c = \varepsilon_0 \omega_p^2 E_\phi \end{cases}, \tag{4}$$

$$\begin{pmatrix} J_\rho \\ J_\phi \\ J_z \end{pmatrix} = \varepsilon_0 \begin{pmatrix} \dfrac{\omega_p^2 \omega_c}{\omega_c^2 - (\omega + jv)^2} & \dfrac{jw_p^2(\omega + jv)}{(\omega + jv)^2 - \omega_c^2} & 0 \\ \dfrac{jw_p^2(\omega + jv)}{(\omega + jv)^2 - \omega_c^2} & \dfrac{\omega_p^2 \omega_c}{-\omega_c^2 + (\omega + jv)^2} & 0 \\ 0 & 0 & \dfrac{j\omega_p^2}{\omega + jv} \end{pmatrix} \begin{pmatrix} E_\rho \\ E_\phi \\ E_z \end{pmatrix}. \tag{5}$$

The effective permittivity of the anisotropic dielectric InSb is controlled by the B, which is along the -z-axis direction [39]. the corresponding effective permittivity function is obtained [39]:

$$\varepsilon_{InSb} = \begin{bmatrix} \varepsilon_1 & j\varepsilon_2 & 0 \\ -j\varepsilon_2 & \varepsilon_1 & 0 \\ 0 & 0 & \varepsilon_3 \end{bmatrix}, \tag{6}$$

where [39]

$$\varepsilon_1 = \varepsilon_\infty - \varepsilon_\infty \frac{\omega_p^2(\omega + jv_c)}{\omega[(\omega + jv_c)^2 - \omega_c^2]}, \tag{7}$$

$$\varepsilon_2 = \varepsilon_\infty \frac{i\omega_p^2 \omega_c}{\omega[(\omega + jv_c)^2 - \omega_c^2]}, \tag{8}$$

$$\varepsilon_3 = \varepsilon_\infty - \varepsilon_\infty \frac{\omega_p^2}{\omega(\omega + jv_c)}. \tag{9}$$

The $\omega_p = (e^2 N_e/\varepsilon_0 m^*)^{1/2}$ represents the plasma frequency and m^* is the carrier effective mass that is connected to the electron mass m_e. $m^* = 0.015m_e$ belongs to InSb. $\varepsilon_\infty = 15.68$ is the high-frequency limit permittivity. $\omega_c = eB/m^*$ indicates the electron cyclotron frequency, which is tuned by B. Moreover, the collision frequency v_c, is $6 \times 10^{-5}\omega_p$ [40]. The e and m are on behalf of electron quantity and electron quality, respectively. The plasma density N is written as [40]:

$$N(m^{-3}) = 5.76 \times 10^{20} T^{1.5} \exp[-0.26/(2 \times 8.625 \times 10^{-5} \times T)], \quad (10)$$

By the equation, the T has a great influence on it. Therefore, Eq. (3) can be derived as [39]:

$$\nabla \times \boldsymbol{H} = \varepsilon_{ar} \varepsilon_{\boldsymbol{Insb}} \frac{\partial \boldsymbol{E}}{\partial t}. \quad (11)$$

Considering Maxwell's equations related to H polarization, the governing equations for the electric field E and magnetic field H in the context of Maxwell's equations related to H polarization can be derived as follows [39]:

$$\frac{1}{\rho}\left[\frac{\partial(\rho E_\phi)}{\partial \rho} - \frac{\partial E_\rho}{\partial \phi}\right] = -j\omega\mu_0 H_z, \quad (12)$$

$$\frac{1}{\rho}\frac{\partial H_z}{\partial \phi} = j\omega\varepsilon_0(\varepsilon_1 E_\rho - j\varepsilon_2 E_\phi), \quad (13)$$

$$\frac{\partial H_z}{\partial \rho} = -j\omega\varepsilon_0(\varepsilon_1 E_\phi + j\varepsilon_2 E_\rho). \quad (14)$$

After eliminating the components E_ρ and E_Φ by substituting them with H_z, the following equation can be obtained [39]:

$$\frac{1}{\rho}\frac{1}{\omega\varepsilon_0(\varepsilon_1^2 - \varepsilon_2^2)}\left\{j\varepsilon_1\frac{\partial}{\partial \rho}\rho\frac{\partial H_z}{\partial \rho} - \varepsilon_2\frac{\partial}{\partial \rho}\frac{\partial H_z}{\partial \phi} + \varepsilon_2\frac{\partial}{\partial \phi}\frac{\partial H_z}{\partial \rho} + j\varepsilon_1\frac{1}{\rho}\frac{\partial}{\partial \phi}\frac{\partial H_z}{\partial \phi}\right\} = -j\omega\mu_0 H_z. \quad (15)$$

The angle part of the equation satisfies the following conditions [39]:

$$\frac{d^2\Phi}{d\phi^2} + m^2\Phi = 0, \quad (16)$$

which has a solution in the form of $\Phi \sim e^{jm\varphi}$, and m can be chosen as an integer or zero.

By combining the standard Bessel's equation with Eq. (15), H and E can be gained [39]:

$$H_z(\rho, \phi) = V(\rho)\Phi(\phi) = [\mathrm{A}J_m(k\rho) + \mathrm{B}Y_m(k\rho)]e^{j\omega\phi}, \quad (17)$$

where considering the azimuthal mode m, the Neumann and Bessel functions are separately symbolized by Y_m and J_m.

Substituting Eq. (17) into Eqs. (13) and (14) results in the following two equations [39]:

$$\frac{m}{\rho}V(\rho)e^{jm\varphi} = \omega\varepsilon_0(\varepsilon_1 E_\rho - j\varepsilon_2 E_\varphi) \quad (18)$$

$$\frac{\partial V}{\partial \rho}e^{j\omega\varphi} = -j\omega\varepsilon_0(\varepsilon_1 E_\varphi + j\varepsilon_2 E_\rho). \quad (19)$$

The following equation can be obtained [39]:

$$E_\phi = \left\{jp\left[AJ_m'(k\rho) + BY_m'(k\rho)\right] - \frac{jm\varepsilon_2}{\omega\varepsilon_0\rho(\varepsilon_1^2 - \varepsilon_2^2)}\left[AJ_m'(k\rho) + BY_m(k\rho)\right]\right\}e^{jm\phi}. \quad (20)$$

The expressions that define the relevant quantities are as follows [39]:

$$E_\phi = U(\rho)e^{jm\phi}. \quad (21)$$

In addition, the forms of $V(\rho)$ and $U(\rho)$ can be respectively calculated as follows [39]:

$$V(\rho) = AJ_m(k\rho) + BY_m(k\rho), \quad (22)$$

$$U(\rho) = jp[AJ_m'(k\rho) + BY_m'(k\rho)] - \frac{jm\varepsilon_2}{\omega\varepsilon_0\rho(\varepsilon_1^2 - \varepsilon_2^2)}[AJ_m(k\rho) + BY_m(k\rho)], \quad (23)$$

where $p = (\mu/\varepsilon_0/\varepsilon_{\mathrm{InSb}})^{1/2}\cos\theta$, $k = \omega p(\varepsilon_1^2\text{-}\varepsilon_2^2)\ \varepsilon_0/\ \varepsilon_1$.

As for InSb, the permittivity is [39]:

$$\varepsilon_{\mathrm{InSb}} = (\varepsilon_1^2 - \varepsilon_2^2)/\varepsilon_1, \quad (24)$$

and the refractive index of the InSb is [39]:

$$n_{\mathrm{InSb}} = (\varepsilon_{\mathrm{InSb}})^{1/2}. \quad (25)$$

When considering different radii of the same dielectric, the relationship between U and V can be described by a second-order transfer matrix in the following form [39]:

$$\begin{bmatrix} V(\rho_i) \\ U(\rho_i) \end{bmatrix} = \mathbf{M}_j \begin{bmatrix} V(\rho_{i-1}) \\ U(\rho_{i-1}) \end{bmatrix}, \quad (26)$$

where $\rho_0 = 0.07d$ is the core radius, and ρ_f is the outermost radius. j donated by A, B, C, D, InSb, and cavity, symbolizes the different dielectric layers.

The the transfer matrix of InSb symbolized $\mathrm{M_{InSb}}$ can be depicted as [39]:

$$\boldsymbol{M}_{\mathrm{InSb}} = \begin{pmatrix} M_{11} & M_{12} \\ M_{21} & M_{22} \end{pmatrix}. \quad (27)$$

Then, according to $J_m(k\rho_0)Y_\mathrm{m}'(k\rho_0)\text{-}J_\mathrm{m}'(k\rho_0)Y_\mathrm{m}(k\rho_0) = 2/(\pi k\rho)$ [39],

$$M_{11} = \left[-\frac{\pi m\varepsilon_2}{2\varepsilon_1}Y_m(k\rho_0) + \frac{\pi}{2}k\rho_0 Y_m'(k\rho_0)\right]J_m(k\rho) + \left[\frac{\pi m\varepsilon_2}{2\varepsilon_1}J_m(k\rho_0) - \frac{\pi}{2}k\rho_0 J_m'(k\rho_0)\right]Y_m(k\rho), \quad (28)$$

$$M_{12} = j\frac{\pi}{2}\frac{k}{p}\rho_0 \cdot [Y_m(k\rho_0)J_m(k\rho) - J_m(k\rho_0)Y_m(k\rho)], \quad (29)$$

$$M_{21} = \left[-\frac{\pi m\varepsilon_2}{2\varepsilon_1}Y_m(k\rho_0) + \frac{\pi}{2}k\rho_0 Y_m'(k\rho_0)\right]\left[jpJ_m'(k\rho) - \frac{jm\varepsilon_2}{\omega\varepsilon_0\rho(\varepsilon_1^2 - \varepsilon_2^2)}J_m(k\rho)\right] + \left[\frac{\pi m\varepsilon_2}{2\varepsilon_1}J_m(k\rho_0) - \frac{\pi k\rho_0}{2}J_m'(k\rho_0)\right]\left[jpY_m'(k\rho) - \frac{jm\varepsilon_2}{\omega\varepsilon_0\rho(\varepsilon_1^2 - \varepsilon_2^2)}Y_m(k\rho)\right], \quad (30)$$

$$M_{22} = -\frac{\pi}{2}k\rho_0 \cdot Y_m(k\rho_0)[J_m'(k\rho) - \frac{m\varepsilon_2}{\omega\varepsilon_0 p\rho(\varepsilon_1^2 - \varepsilon_2^2)} \cdot J_m(k\rho)] - \frac{\pi}{2}k\rho_0 \cdot J_m(k\rho_0)[Y_m'(k\rho) - \frac{m\varepsilon_2}{\omega\varepsilon_0 p\rho(\varepsilon_1^2 - \varepsilon_2^2)}Y_m(k\rho)]. \quad (31)$$

Under TM polarization, $k_{\mathrm{InSb}} = \omega/cn_{\mathrm{InSb}}\cos\theta_{\mathrm{InSb}}$ is the wave vector component in the Φoz-plane and $\eta = (\varepsilon_0/\mu_0)^{1/2}n_{\mathrm{InSb}}/\cos\theta$ is the light conductivity. For ordinary dielectrics that are unaffected by B, their transfer matrix can be expressed as follows [39]:

$$M_j = \begin{pmatrix} m_{11} & m_{12} \\ m_{21} & m_{22} \end{pmatrix}, \quad (32)$$

$$m_{11} = \frac{\pi}{2}k_i\rho_{i-1}[Y_m'(k_i\rho_{i-1})J_m(k_i\rho_i) - J_m'(k_i\rho_{i-1})Y_m(k_i\rho_i)], \quad (33)$$

$$m_{12} = -j\frac{\pi}{2}\frac{k_i}{p_i}\rho_{i-1}[J_m(k_i\rho_{i-1})Y_m(k_i\rho_i) - Y_m(k_i\rho_{i-1})J_m(k_i\rho_i)], \quad (34)$$

$$m_{21} = j\frac{\pi}{2}k_i p_i \rho_{i-1}[Y_m'(k_i\rho_{i-1})J_m'(k_i\rho_i) - J_m'(k_i\rho_{i-1})Y_m'(k_i\rho_i)], \quad (35)$$

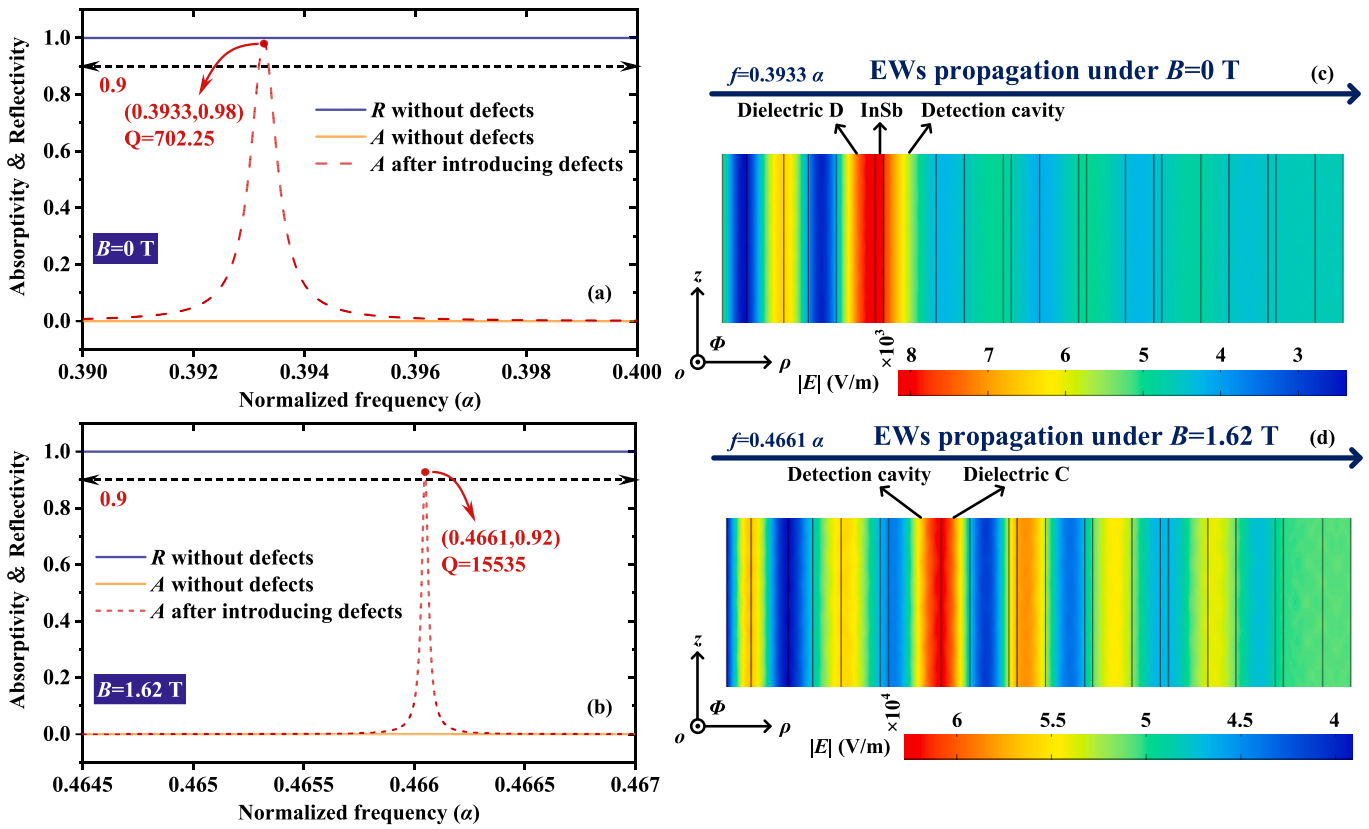

Fig. 2. The A and R maps under the influence of defects when (a) $B = 0$ T, and (b) $B = 1.62$ T. The electric field distribution diagram in the $+\rho$ direction when (c) $f = 0.3933\ \alpha$ and $B = 0$ T, and (d) $f = 0.4661\ \alpha$ and $B = 1.62$ T.

$$m_{22} = \frac{\pi}{2} k_i \rho_{i-1} [J_m(k_i \rho_{i-1}) Y_m'(k_i \rho_i) - Y_m(k_i \rho_{i-1}) J_m'(k_i \rho_i)]. \tag{36}$$

where i indicated by A, B, C, D, and cavity, represents the different ordinary dielectrics. $k_i = \omega/c n_i \sin\theta_i$ is the wave vector component on the $+\rho$-axis. Here is the complete positive transfer matrix M [39]:

$$\mathrm{M} = \mathrm{M_A M_B M_A M_C M_D M_{InSb} M_{cavity} (M_C M_D M_{InSb})^2 M_D M_C M_{InSb} M_D M_C M_D M_{InSb} M_D M_C}, \tag{37}$$

$$\mathrm{M}^{-1} = \begin{pmatrix} M_{11} & M_{12} \\ M_{21} & M_{22} \end{pmatrix}^{-1} = \frac{1}{\mathrm{detM}} \begin{pmatrix} M_{22} & -M_{12} \\ -M_{21} & M_{11} \end{pmatrix} = \begin{pmatrix} M_{11}' & M_{12}' \\ M_{21}' & M_{22}' \end{pmatrix}, \tag{38}$$

where the specific expressions belonging to M can be derived from the transfer matrixes of different dielectrics, which are indicated in Eqs. (27)–(36). Furthermore, in Eq. (38), "det" symbolizes the determinant of the matrix. When TM EWs propagate through dielectric InSb layers, the transfer matrices are donated as $\mathrm{M_{InSb}}$, and their explicit expressions are shown as Eqs. (27)–(31).

The reflection coefficient r and transmittance coefficient t of the CMS can be expressed as [39]:

$$r = \frac{(M_{21}' + jp_0 C_{m0}^{(2)} M_{11}') - jp_f C_{mf}^{(2)} (M_{22}' + jp_0 C_{m0}^{(2)} M_{12}')}{-(jp_0 C_{m0}^{(1)} M_{11}' + M_{21}') + jp_f C_{mf}^{(2)} (jp_0 C_{m0}^{(1)} M_{12}' + M_{22}')}, \tag{39}$$

$$t = \frac{-4\varepsilon_r^{-1} \sqrt{\frac{\mu_0}{\varepsilon_0}}}{\pi K \rho_0 H_m^{(2)}(k\rho_0) H_m^{(1)}(k\rho_0) [-(jp_0 C_{m0}^{(1)} M_{11}' + M_{21}') + jp_f C_{mf}^{(2)} (jp_0 C_{m0}^{(1)} M_{12}' + M_{22}')]}. \tag{40}$$

The values of reflectance (R) and transmittance (T) can be calculated as [40,41]:

$$R = |r|^2, \tag{41}$$

$$T = |t|^2. \tag{42}$$

Then, the absorptivity (A) can be gained [40,41]:

$$A = 1 - R - T \tag{43}$$

3. Numerical results and discussion

The multitasking performance of the renal function assessment biosensor proposed is discussed below. To explain the generation principle of sharp AP which is used for RI detection, the A and R spectra are presented in Fig. 2(a) and (b), when EWs enter into CMS under the influence of different B and defects. The cases of injection of different analytes into the detection cavity are discussed. As exhibited in Fig. 2(a), under the condition that $B = 0$ T and $n_{\mathrm{cavity}} = 1.3323$, when the defects are not introduced into CMS, it can be seen from R approximately 1 and

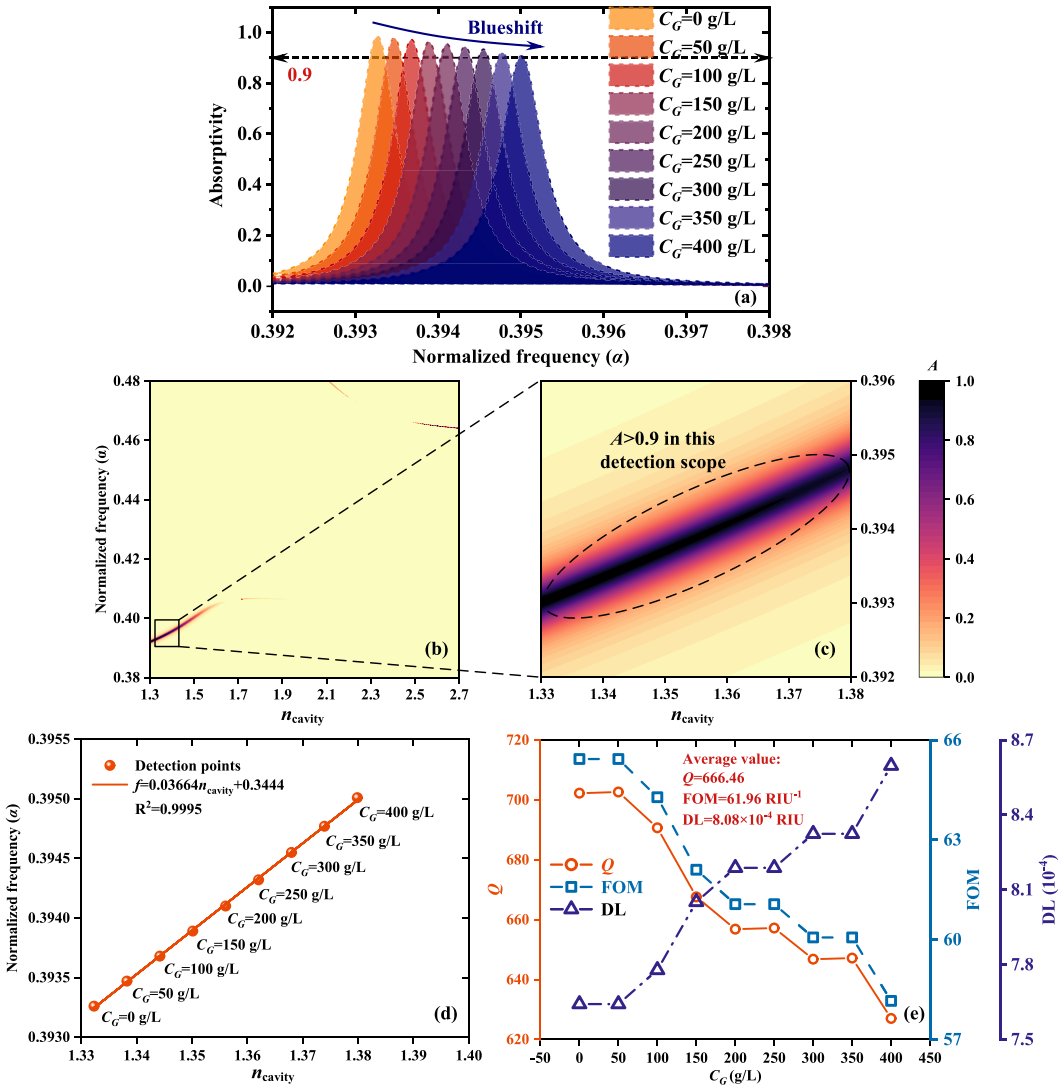

Fig. 3. Schematic diagrams of the C_G detection under $B = 0$ T. (a) The AP belonging to the C_G of 0 ~ 400 g/L, changing at equal interval of 50 g/L. (b) The top view of A curves under $n_{cavity} = 1.3 \sim 2.7$, and (c) the enlarged diagram under $n_{cavity} = 1.33 \sim 1.38$. (d) The LFR between normalized frequency and n_{cavity}. (e) The Q, FOM and DL belonging to different C_G detection points.

A infinitely close to 0 that the photonic band gap is formed between frequencies f of 0.39 ~ 0.4 α, blocking the propagation of EWs. When the defects are introduced, the original structure is broken and an absorption band is formed in the original photonic band gap [28]. Thus, sharp AP of $A = 0.98$ and Q = 702.25 is generated at $f = 0.3933$ α. When $B = 1.62$ T and $n_C = 2.565$, similarly, a photonic band gap is formed in the frequency band of 0.4645 ~ 0.467 α in Fig. 2(b). The introduction of the defects produces a sharp AP of $A = 0.92$ at $f = 0.4661$ α. Notably, it has a higher Q of 15,535 than that in the case of $B = 0$ T. To more clearly observe the EWs propagation in the structure under TM polarization, the distributions of electric field energy corresponding to $B = 0$ T and $B = 1.62$ T are presented in Fig. 2(c) and (d). When EWs enter CMS at $f = 0.3933$ α, the electric field energy is localized and enhanced on the InSb defect layer surface in Fig. 2(c), $|E|$ reaches 10^3 V/m level, LDMR is excited, and AP sharply increases. When EWs of $f = 0.4661$ α propagate in CMS, Fig. 2(d) exhibits that the electric field energy is localized at the layers surfaces of the detection cavity and dielectric C, LDMR is excited, and sharp AP is generated. Compared with the cases of Fig. 2(c), the electric field energy $|E|$ under this condition reaches the level of 10^5 V/m. A larger $|E|$ means a sharper AP [42], which explains the phenomenon that the Q of AP in Fig. 2(d) is larger than that of AP in Fig. 2(c).

Modulations of f, phase. and amplitude are common methods of sensor operation. Among these, f modulation is the most extensively utilized method owing to its convenient application in experiments and observations. By establishing a unique linear relationship between the f and the measured variable (the physical quantity is difficult to directly detect), and forming a one-to-one correspondence relationship, the signal that is not easy to observe is converted into the photoelectric signal that is convenient to detect. The renal function assessment biosensor designed in this work is also predicated on this mechanism. As the EWs propagate towards the detection region, which is the detection cavity, the f position of the resonant AP caused by defects can be shifted by altering the concentration of the analyte being detected. This movement also establishes a one-to-one correspondence through f locking of AP, thereby achieving the goal of determining the concentration of the analyte being detected. In addition, since the dielectric InSb regulated by the is introduced into CMS, the change of B will alter the RI of the InSb layer, thus affecting the equivalent RI and impedance of the whole CMS. The wave vector and phase of the EWs propagating in the CMS are hence affected, which reflects that the A of AP in the same f range will be diverse under different B. Taking advantage of this interesting phenomenon, the AP of $A > 0.9$ is set as the standard that can be used for detection. Through the regulation of B, biosensing of detected analyte with different RI can be realized, expanding the range of RI

Table 2
The C_C (μmol/L) with attributed RI [16].

C_C (μmol/L)	RI
85.28	2.565
84.07	2.589
83.3	2.610
82.3	2.639
81.43	2.655
80.9	2.661

detection and types of biosensing.

In the absence of an externally applied magnetic field ($B = 0$ T), CMS can perform RI detection on C_G from 0 g/L to 400 g/L, as shown in Fig. 3. Hollow submicron size pipettes are used to accurately inject the measured concentration of glucose solution into the detection cavity [23]. The relationship between detection cavity RI n_{cavity} and C_G can be expressed as [25]:

$$n_{cavity} = 1.33230545 + 0.00011889 C_G. \tag{44}$$

As shown in Fig. 3(a), when C_G increases at an equal interval of 50 g/L within the range of 0 ~ 400 g/L, the f of the corresponding sharp AP will gradually move to the direction of high f, resulting in a blue shift phenomenon. 0.3933 α, 0.3935 α, 0.3937 α, 03,939 α, 0.3941 α, 0.3943 α, 0.3946 α, 0.3948 α, 0.395 α are the corresponding normalized frequencies, respectively. To more intuitively show that B regulates the CMS RI detection range, Fig. 3(b) indicates the top view of the three-dimensional curve representing the variation of A when the n_{cavity} continuously changes within the range of 1.3 ~ 2.7. It can be seen that only in the n_{cavity} range of 1.3 ~ 1.65 there are continuous changes of AP that satisfy the detection condition ($A > 0.9$). Fig. 3(c) displays that the enlarged figure contains the RI range of 1.3323 ~ 1.3799 corresponding to C_G of 0 ~ 400 g/L. In the RI range of 1.33 ~ 1.38, the n_{cavity} increases continuously at the interval of 1×10^{-5} RIU, obviously existing the AP blueshift with $A > 0.9$, which meets the A requirement of RI detection.

S, Q, FOM, and DL are introduced as important indexes to assess the sensor performance. Excellent sensors correspond to higher S, Q, FOM, and lower DL. The relevant expressions are written as [43]:

$$S = \frac{\Delta f}{\Delta x}, \tag{45-a}$$

$$Q = \frac{f_T}{FWHM}, \tag{45-b}$$

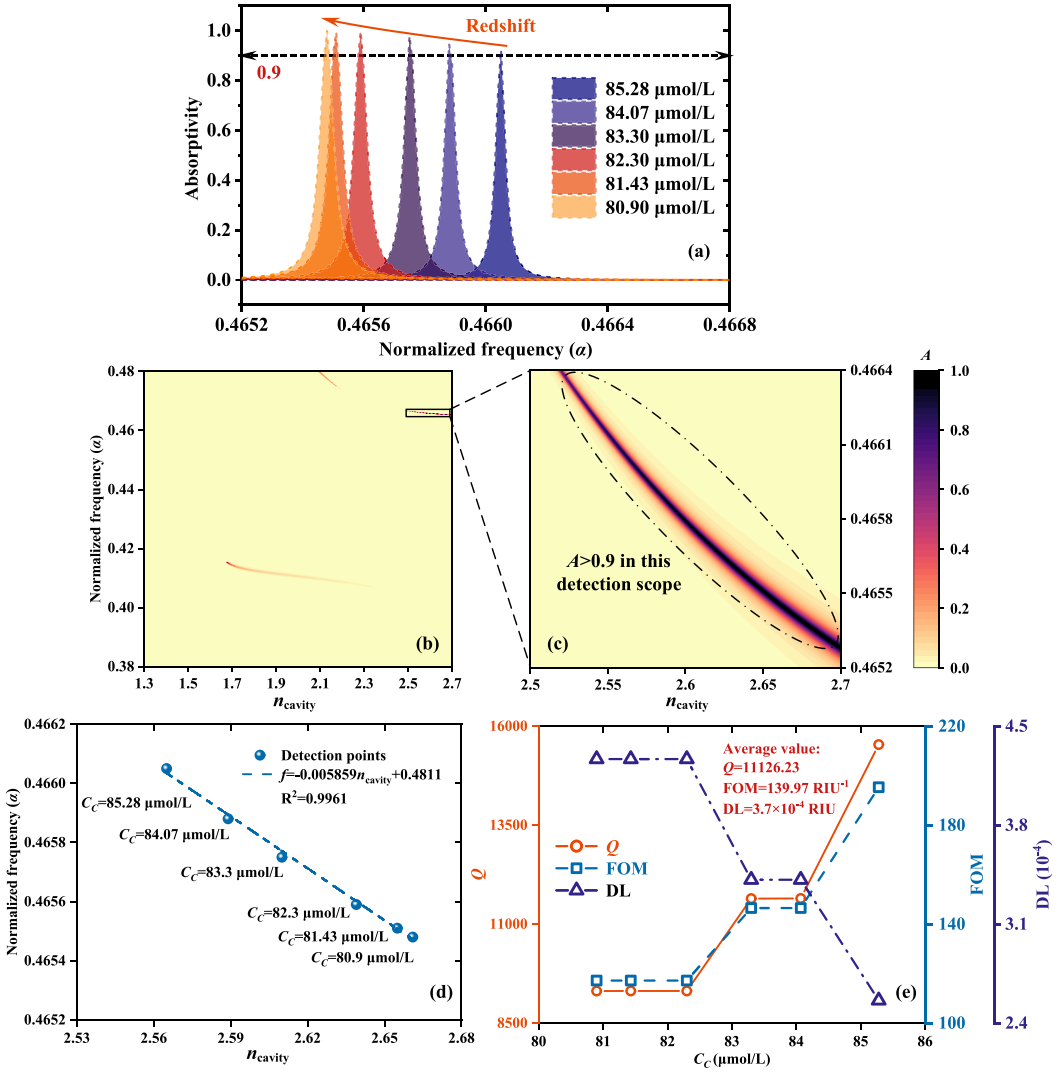

Fig. 4. Schematic diagrams of the C_C detection under $B = 1.62$ T. (a) The AP belonging to the different C_C points in the range of 80.9 ~ 85.28 μmol/L. (b) The top view of A curves under $n_{cavity} = 1.3 \sim 2.7$, and (c) the enlarged diagram under $n_{cavity} = 2.5 \sim 2.7$. (d) The LFR between normalized frequency and n_{cavity}. (e) The Q, FOM and DL belonging to different C_C detection points.

Table 3
The published reports compared with the proposed CMS in terms of the performance.

Refs.	Multitasking	Quantity	Range	S	Q	FOM
[13]	×	C_G	0 ~ 300 g/L	22 THz/RIU	800	0.3865 RIU^{-1}
[11]	×	C_G	0 ~ 200 g/L	36 THz/RIU	16.5	19 RIU^{-1}
[45]	×	C_G	0 ~ 250 g/L	500 nm/RIU	50	11.82 RIU^{-1}
[46]	×	C_G	0 ~ 350 g/L	4.72 THz/RIU	32.49	14 RIU^{-1}
[16]	×	C_C	80.9 ~ 85.28 μmol/L	306.25 nm/RIU	39,000	15,000 RIU^{-1}
[47]	×	C_C	0 ~ 2000 μM	0.0025 nm/μM	\	389.41 M^{-1}
[48]	×	C_C	0 ~ 2000 μg/mL	0.41 nm/(μg/mL)	1380	0.0269 mL/μg
[49]	×	C_C	0.7 ~ 1.1 mg/dL	8.18 A dL/g	\	\
This work	√	C_G	0 ~ 400 g/L	6.91 THz/RIU	666.46	61.96 RIU^{-1}
		C_C	80.9 ~ 85.28 μmol/L	1.104 THz/RIU	11126.23	139.97 RIU^{-1}

$$DL = \frac{f_T}{20SQ}. \tag{45-c}$$

$$FOM = \frac{S}{FWHM}, \tag{45-d}$$

where Δf and Δx represent the increment of AP f and the change of analyte physical quantity, respectively. The f of AP and half-height of AP are separately expressed by f_T and full width at half-height (FWHM). To more clearly show the detection performance of CMS, the linear fitting relationship (LFR) is obtained by using the linear fitting method corresponding to the detection points taken in Fig. 3(a). Fig. 3(d) exhibits the LFR of AP f points and n_{cavity}, $f = 0.03664n_{cavity} + 0.3444$. 0.03664 α/THz is S, and when $d = 10$ μm, S = 6.91 THz/RIU. The introduction of R^2 allows for the evaluation of the goodness of fit in linear regression. $R^2 = 0.9995$ indicates LFR has high reliability, and the error between the value obtained by the fitting curve and the actual measured value is small. Fig. 3(e) displays the performance evaluation of each detection point. With the C_G increase, Q and FOM belonging to AP gradually decrease, while DL gradually rises. The mean values belonging to Q, FOM, and DL are 66.46, 61.96 RIU^{-1}, and 8.08×10^{-4} RIU. Compared to the infrared C_G-sensitive biosensor with FOM of 0.3865 RIU^{-1} [13], and the plasma ring nanobiosensor for measuring C_G with a detection range of 0 ~ 200 g/L and Q of 16.5 [11], the biosensor designed in this work has a wider C_G detection range, lower loss and more conducive to the accurate detection of C_G with a strong resolution, offering a new possibility for the precise observation of blood glucose concentration in medicine to assess renal function.

Table 2 shows the relationship between serum C_C and RI [16]. With the decrease of C_C, the belonging RI increases. Under the condition of the existence of an externally applied magnetic field strength $B = 1.62$ T, an unknown concentration of serum creatinine solution is injected into the detection cavity [23]. By locating the f points of sharp AP, the RI detection of 80.9 ~ 85.28 μmol/L C_C can be accurately performed. This plays a crucial role in the diagnosis of renal disease [44].

Corresponding to the concentration and RI in Table 2, Fig. 4(a) presents A spectra under different C_C. In the process of raising the n_{cavity} from 2.565 to 2.661, the corresponding f of AP is 0.4661 α, 0.4659 α, 0.4658 α, 0.4656 α, 0.4655 α, and 0.46548 α, respectively. It is found that with the decrease of C_C, that is, the increase of n_{cavity}, AP produced a redshift phenomenon and moved to the high f direction. For the top view of the three-dimensional change curve of A when the n_{cavity} changes continuously in the range of 1.3 ~ 2.7, compared with a continuous change AP curve with $A > 0.9$ existing in the $n_{cavity} = 1.3 \sim 1.65$ under the condition of $B = 0$ T in Fig. 3(b), Fig. 4(b) shows that the color belonging to the same $n_{cavity} = 1.3 \sim 1.65$ region is yellow. According to the legend, it means that A of AP approaches 0 infinitely, which does not meet the detection requirements. On the contrary, in the enlarged diagram Fig. 4(c), there is a good linear change curve belonging to AP with $A > 0.9$ in the n_{cavity} range of 2.53 ~ 2.7, also covering the range of detected serum creatinine RI from 2.565 to 2.661. The LFR is shown in Fig. 4(d), $f = -0.005859n_{cavity} + 0.4811$. S = 0.005859 α/RIU, when the normalized thickness $d = 10$ μm, S = 1.104 THz/RIU. Compared with $R^2 = 0.9132$ for C_C biosensors based on one-dimensional planar photonic crystals [16], the LFR of detection points in this work has $R^2 = 0.9961$, indicating the reliability of C_C detection. The Q, FOM, and DL of AP under each C_C are exhibited in Fig. 4(a), the corresponding average values are 11126.23, 139.97 RIU^{-1}, and 3.7×10^{-4} RIU. High values of Q, FOM, and low values of DL mean that the C_C detection error of CMS is small and the resolution is high.

To systematically and intuitively demonstrate the advantages of the proposed renal function assessment biosensor based on CMS, previous biosensors with excellent performance are listed in Table 3. Compared with them, it can be seen that the designed CMS is able to achieve multitasking, meanwhile also guaranteeing excellent performance, which is generally better than the previous biosensors. Therefore, the biosensor for renal function assessment studied in this paper has a certain advanced nature and value, owning important reference value for promoting the detection and treatment of renal diseases.

4. Conclusion

In conclusion, this paper proposes a multitasking renal function assessment biosensor based on CMS. By introducing InSb, the mode switch of C_G and C_C biosensing can be realized by tuning the B. The multitasking integration of CMS can effectively reduce the cost of multiple single-function sensors and is more suitable for the application of multiple medical detection scenarios. After the method of searching for optimization and reasonable structural design, by locking the f of sharp AP generated by LDMR, C_G of 0 ~ 400 g/L can be detected when B is absent ($B = 0$ T) with S of 6.91 THz/RIU, R^2 of 0.9995, Q of 666.46, FOM of 61.96 RIU^{-1}, and DL of 8.08×10^{-4} RIU. Moreover, the detection has a wider range and more accurate performance than previous C_G biosensors. In the case of $B = 1.62$ T, the C_C of 80.9 ~ 85.28 μmol/L can be detected by the CMS with RI of 80.9 ~ 85.28 μmol/L, with R^2 of 0.9961, which is more reliable than the previous C_C biosensors. Q of 11126.23, FOM of 139.73 RIU^{-1}, and DL of 3.7×10^{-4} RIU also prove its excellent detection performance. The multitasking biosensor proposed for renal function assessment not only has the advantages of the geometric and optical properties of CMS but also has the properties of real-time detection, non-destructive and labeling-free by using the electromagnetic characteristics of EWs for detection. This provides a feasible scheme for accurate and comprehensive assessment, detection, and treatment of renal diseases.

CRediT authorship contribution statement

Jun-Yang Sui: Data curation, Formal analysis, Investigation, Writing – original draft, Visualization. **Jia-Hao Zou:** Software, Validation. **Ding-Yuan Zhang:** Software, Validation. **Si-Yuan Liao:** Software, Validation. **Yu-Xin Wei:** Software, Validation. **Hai-Feng Zhang:** Conceptualization, Supervision, Writing – review & editing,

Methodology.

Declaration of Competing Interest

The authors declare that they have no known competing financial interests or personal relationships that could have appeared to influence the work reported in this paper.

Data availability

Data will be made available on request.

References

[1] D.N. Koye, D.J. Magliano, R.G. Nelson, M.E. Pavkov, The global epidemiology of diabetes and kidney disease, Adv. Chronic Kidney Dis. 25 (2) (2018) 121–132.
[2] R.B. Jain, A. Ducatman, Perfluoroalkyl acids serum concentrations and their relationship to biomarkers of renal failure: serum and urine albumin, creatinine, and albumin creatinine ratios across the spectrum of glomerular function among US adults, Environ. Res. 174 (2019) 143–151.
[3] K. Kashani, M.H. Rosner, M. Ostermann, Creatinine: from physiology to clinical application, Eur. J. Intern. Med. 72 (2020) 9–14.
[4] J. Tossenberger, M. Rademacher, K. Németh, V. Halas, A. Lemme, Digestibility and metabolism of dietary guanidino acetic acid fed to broilers, Poult. Sci. 95 (2016) 2058–2067.
[5] C.-T.-S. Ching, T.-P. Sun, D.-Y. Jheng, H.-W. Tsai, H.-L. Shieh, A creatinine biosensor based on admittance measurement, Biosens. Nanomed. VIII SPIE. 9550 (2015) 97–100.
[6] J.H.T. Luong, K.B. Male, J.D. Glennon, Biosensor technology: technology push versus market pull, Biotechnol. Adv. 26 (2008) 492–500.
[7] A. Diouf, S. Motia, N. El Alami El Hassani, N. El Bari, B. Bouchikhi, Development and characterization of an electrochemical biosensor for creatinine detection in human urine based on functional molecularly imprinted polymer, J. Electroanal. Chem. 788 (2017) 44–53.
[8] P.K. Verma, H. Lee, J.-Y. Park, J.-H. Lim, M. Maj, J.-H. Choi, K.-W. Kwak, M. Cho, Modulation of the hydrogen bonding structure of water by renal osmolytes, J. Phys. Chem. Lett. 6 (2015) 2773–2779.
[9] S. Yadav, R. Devi, A. Kumar, C.S. Pundir, Tri-Enzyme Functionalized ZnO-NPs/CHIT/c-MWCNT/PANI composite film for amperometric determination of creatinine, Biosens. Bioelectron. 28 (2011) 64–70.
[10] A. Capozzi, S. Patel, W.T. Wenckebach, M. Karlsson, M.H. Lerche, J.H. Ardenkjær-Larsen, Gadolinium effect at high-magnetic-field DNP: 70% 13C polarization of [U-13C] glucose using trityl, J. Phys. Chem. Lett. 10 (2019) 3420–3425.
[11] S. Ghorbani, M. Sadeghi, Z. Adelpour, A highly sensitive and compact plasmonic ring nano-biosensor for monitoring glucose concentration, Laser Phys. 30 (2) (2020) 026204.
[12] S. Robinson, N. Dhanlaksmi, Photonic crystal based biosensor for the detection of glucose concentration in urine, Photonic Sens. 7 (2017) 11–19.
[13] S.K. Chamoli, S.C. Singh, C. Guo, Design of extremely sensitive refractive index sensors in infrared for blood glucose detection, IEEE Sens. J. 20 (2020) 4628–4634.
[14] V. Barone, Accuracy meets feasibility for the structures and rotational constants of the molecular bricks of life: a joint venture of DFT and wave-function methods, J. Phys. Chem. Lett. 14 (2023) 5883–5890.
[15] P. Kumar, R. Jaiwal, C.S. Pundir, An Improved amperometric creatinine biosensor based on nanoparticles of creatininase, creatinase and sarcosine oxidase, Anal. Biochem. 537 (2017) 41–49.
[16] H. Aly, D. Mohamed, M.A. Mohaseb, N.S. Abd El-Gawaad, Y. Trabelsi, Biophotonic sensor for the detection of creatinine concentration in blood serum based on 1D photonic crystal, RSC Adv. 10 (2020) 31765–31772.
[17] M. Mansouree, H. Kwon, E. Arbabi, A. McClung, A. Faraon, A. Arbabi, Multifunctional 2.5D metastructures enabled by adjoint optimization, Optica, OPTICA 7 (2020) 77–84.
[18] M.-S. Chen, C.-J. Wu, T.-J. Yang, Wave properties of an annular periodic multilayer structure containing the single-negative materials, Phys. Lett. A 373 (2009) 3594–3600.
[19] S.A. El-Naggar, Photonic gaps in one dimensional cylindrical photonic crystal that incorporates single negative materials, Eur. Phys. J. D 71 (2017) 1–6.
[20] D.R. Smith, D. Schurig, Electromagnetic wave propagation in media with indefinite permittivity and permeability tensors, Phys. Rev. Lett. 90 (2003) 077405.
[21] J.X. Zhao, J.J. Cheng, Y.Q. Chu, Y.X. Wang, F.G. Deng, Q. Ai, Hyperbolic metamaterial using chiral molecules, Sci. China Phys. Mech. Astron. 63 (6) (2020) 260311.
[22] S. Gandhi, S. Kumar Awasthi, H. Aly, Biophotonic sensor design using a 1D defective annular photonic crystal for the detection of creatinine concentration in blood serum, RSC Adv. 11 (2021) 26655–26665.
[23] P. Russell, Photonic crystal fibers, Science 299 (2003) 358–362.
[24] M.M. Abadla, H.A. Elsayed, A. Mehaney, Novel design for the temperature sensing using annular photonic crystals, Silicon 13 (2021) 4737–4745.
[25] A. Mehaney, M.M. Abadla, H.A. Elsayed, 1D porous silicon photonic crystals comprising Tamm/Fano resonance as high performing optical sensors, J. Mol. Liq. 322 (2021) 114978.
[26] A. Sills, P. Harrison, M. Califano, Exciton dynamics in InSb colloidal quantum dots, J. Phys. Chem. Lett. 7 (2016) 31–35.
[27] B.H. Cheng, H.W. Chen, K.J. Chang, Y.-C. Lan, D.P. Tsai, Magnetically controlled planar hyperbolic metamaterials for subwavelength resolution, Sci. Rep. 5 (2015) 18172.
[28] S.-S. Rao, J.-T. Zhang, H.-F. Zhang, A multifunctional and multiscale device of magnetic-controlled AND logical operation and detection based on the nonreciprocity of the magnetized InSb photonic structure, Results Phys. 31 (2021) 105058.
[29] F. Segovia-Chaves, H.A. Elsayed, A. Mehaney, Tunability in the terahertz range of a one-dimensional photonic quasicrystal containing an InSb semiconductor, Optik 245 (2021) 167675.
[30] E. Keshock, P. Peng, J. Zhou, D. Talbayev, Nonreciprocal fabry-perot effect and performance enhancement in a magneto-optical InSb-based faraday terahertz isolator, Opt. Express, OE. 28 (2020) 38280–38292.
[31] M.-S. Chen, C.-J. Wu, T.-J. Yang, Optical properties of a superconducting annular periodic multilayer structure, Solid State Commun. 149 (2009) 1888–1893.
[32] S.K. Srivastava, A. Aghajamali, Investigation of reflectance properties in 1D ternary annular photonic crystal containing semiconductor and high-Tc superconductor, J. Supercond. Nov. Magn. 29 (2016) 1423–1431.
[33] W.M.J. Green, J. Scheuer, G. DeRose, A. Yariv, Vertically emitting annular bragg lasers using polymer epitaxial transfer, Appl. Phys. Lett. 85 (2004) 3669–3671.
[34] J. Scheuer, A. Yariv, Annular bragg defect mode resonators, J. Opt. Soc. Am. B, JOSAB. 20 (2003) 2285–2291.
[35] L. Lewin, The electrical constants of a material loaded with spherical particles, Proc. Inst. Electr. Eng. III Radio Commun. Eng. 94 (1947) 65–68.
[36] X. Liu, Q. Zhao, C. Lan, J. Zhou, Isotropic Mie resonance-based metamaterial perfect absorber, Appl. Phys. Lett. 103 (2013).
[37] F. Intonti, S. Vignolini, V. Türck, M. Colocci, P. Bettotti, L. Pavesi, S.L. Schweizer, R. Wehrspohn, D. Wiersma, Rewritable photonic circuits, Appl. Phys. Lett. 89 (2006) 211117.
[38] F. Fan, S.-J. Chang, W.-H. Gu, X.-H. Wang, A.-Q. Chen, Magnetically tunable terahertz isolator based on structured semiconductor magneto plasmonics, IEEE Photon. Technol. Lett. 24 (2012) 2080–2083.
[39] Q.-Y. Wang, S. Liu, D.i. Gui, H.-F. Zhang, Nonreciprocal absorption characteristics of one-dimensional cylindrical magnetized plasma photonic crystals, Phys. Scr. 96 (6) (2021) 065501.
[40] M.S. Chen, C.J. Wu, T.J. Yang, Optical properties of a superconducting annular periodic multilayer structure, Solid State Commun. 149 (2019) 1888–1893.
[41] S.K. Srivastava, A. Aghajamali, Investigation of reflectance properties in 1D ternary annular photonic crystal containing semiconductor and high-Tc superconductor, J. Supercond. Nov. Magn. 29 (2016) 1423–1431.
[42] T. Cui, X. Liu, L. Zhou, S. Feng, X. Chen, H. Guo, C. Li, Y. Wang, A High-performance refractive index sensor based on a triangular-lattice photonic crystal with defect and surface modes, Laser Phys. 30 (1) (2020) 016209.
[43] Z.A. Zaky, A.M. Ahmed, A.S. Shalaby, A.H. Aly, Refractive index gas sensor based on the Tamm state in a one-dimensional photonic crystal: theoretical optimisation, Sci. Rep. 10 (2020) 9736.
[44] J. Raveendran, P.E. Resmi, T. Ramachandran, B.G. Satheesh, T.G. Babu, Fabrication of a disposable non-enzymatic electrochemical creatinine sensor, Sens. Actuators B 243 (2017) 589–595.
[45] A. Asim, M. Cada, Design of a plasmonic metasurface for refractive index sensing of aqueous glucose, PIER Lett. 107 (2017) 133–139.
[46] M. Karthikeyan, P. Jayabala, S. Ramachandran, S.S. Dhanabalan, T. Sivanesan, M. Ponnusamy, Tunable optimal dual band metamaterial absorber for high sensitivity THz refractive index sensing, Nanomaterials 12 (2022) 2693.
[47] M. Li, R. Singh, C. Marques, B. Zhang, S. Kumar, 2D Material assisted SMF-MCF-MMF-SMF based LSPR sensor for creatinine detection, Opt. Express, OE. 29 (2021) 38150–38167.
[48] S. Sharma, A.M. Shrivastav, B.D. Gupta, Lossy mode resonance based fiber optic creatinine sensor fabricated using molecular imprinting over nanocomposite of MoS2/SnO2, IEEE Sens. J. 20 (2020) 4251–4259.
[49] M.A.A. Khushaini, N.H. Azeman, C.-H. Teh, R. Daik, A.G. Ismail, B.Y. Majlis, M. M. Salleh, W.A.H.W.M. Adnan, T.H.T.A. Aziz, A.A.A. Bakar, A.R.M. Zain, Electrochemical metallization process on screen-printed electrode for creatinine monitoring application, IEEE Sens. J. 22 (2022) 9268–9275.